Dongjie Tang[1, 2], Xuewu Fu[3], Xiaoying Shi[1, 4], Limin Zhou[5], Wang Zheng[6], Chao Li[5], Dongtao Xu[4], Xiqiang Zhou[7, 8], Baozeng Xie[1, 2], Xiyan Zhu[9], and Ganqing Jiang[10]

[1]State Key Laboratory of Biogeology and Environmental Geology, China University of Geosciences (Beijing), Beijing 100083, China

[2]Institute of Earth Sciences, China University of Geosciences (Beijing), Beijing 100083, China

[3]State Key Laboratory of Environmental Geochemistry, Institute of Geochemistry, Chinese Academy of Sciences, 46 Guanshui Road 550002, Guiyang, China

[4]School of Earth Sciences and Resources, China University of Geosciences (Beijing), Beijing 100083, China

[5]National Research Center for Geoanalysis, Beijing 100037, China

[6]Institute of Surface-Earth System Science, School of Earth System Science, Tianjin University, Tianjin, TJ, 300072, China

[7]Key Laboratory of Cenozoic Geology and Environment, Institute of Geology and Geophysics, Chinese Academy of Sciences, Beijing, China

[8]University of Chinese Academy of Sciences, Beijing 100049, China

[9]Institute of Geology and Geophysics, Chinese Academy of Sciences, Key Laboratory of Mineral Resources Research, Chinese Academy of Sciences, Beijing 100029, China

[10]Department of Geoscience, University of Nevada, Las Vegas, NV 89154-4010, USA

Corresponding author: D. Tang (dongjtang@126.com), X. Fu (fuxuewu@mail.gyig.ac.cn)

Key Points:

- Hg-enrichment recognized in the middle Gaoyuzhuang Formation, North China, coincides with the transient oxygenation event at ~1.57 Ga.
- Positive ^{202}Hg, Rb/Al and negative $\Delta^{199}Hg$ shifts suggest that the enrichment was resulted from enhanced continent weathering.
- Enhanced weathering may have increased phosphorous input and primary production in the ocean, thus triggering the oxygenation event.

Abstract

The mid-Proterozoic (~1.8–0.8 Ga) is characterized by low atmospheric oxygen and pervasive oceanic anoxia, with transient oxygenations. One of the prominent oxygenation events happened at ~1.57 Ga, during which atmospheric O_2 may have reached 4% present atmospheric level (PAL) and thus promoted the evolution of multi-cellular eukaryotes. The causes for this oxygenation event, however, remained unknown. Here, we report the result of ^{202}Hg and ^{199}Hg,

P concentration, Rb/Al, and $_{Nd}$(t) across this oxygenation interval in the Gaoyuzhuang Formation of North China. The positive ^{202}Hg, $_{Nd}$(t), and negative Δ^{199}Hg shifts, and the accompanied peaks in Rb/Al, P and I/(Ca+Mg) suggest that this oxygenation was likely resulted from enhanced weathering of intermediate to mafic rocks, which may have promoted primary production via increasing P influx to the ocean and led to the rise in oxygen levels. The data indicate that enhanced weathering input can trigger transient oxygenation events during the mid-Proterozoic.

Plain Language Summary (<200 words)

During mid-Proterozoic (~1.8–0.8 Ga), the oxygen concentrations in atmosphere and shallow seawater were persistently low but occasionally interrupted by transient oxygenation events. The origin of these short oxygenation events, however, is not properly known. To reveal the potential causes behind the events, we take the prominent oxygenation event at ~1.57 Ga as an example to perform Hg isotope, $_{Nd}$(t), major and trace element analyses. The result shows that this oxygenation event is associated with relatively high mass dependent mercury isotope (^{202}Hg), $_{Nd}$(t), Rb/Al and low mass independent mercury isotope (Δ^{199}Hg) values, and an increase in phosphorus concentration as well. The most plausible explanation for these data is that a short-term enhanced continental weathering has resulted in an increase of nutrient input (e.g., phosphorus) to the ocean, stimulating a higher ocean primary production and therefore the transient oxygenation event.

1 Introduction

The oxygenation state of the mid-Proterozoic (~1.8–0.8 Ga) ocean- atmosphere system has been intensively studied in the last decade, and remained highly controversial. Both low (<0.1–1% PAL; Planavsky et al., 2014) and high (>1–4% PAL; Zhang et al., 2016; Canfield et al., 2018) atmospheric O_2 levels have been proposed. Increasing evidence, however, indicates that the mid-Proterozoic redox conditions were highly dynamic, with several intervals of high oxygen levels against an overall low backdrop, including the oxygenation event at ~1.57 Ga (Zhang et al., 2018; Shang et al., 2019). The ~1.57 Ga oxygenation event is characterized by high I/(Ca+Mg) values, positive Cr isotopes coupled with a negative carbon isotope (^{13}C) excursion that was interpreted as the result of dissolved organic carbon (DOC) oxidation in response to increased oxygen (Shang et al., 2019; Xie et al., 2022). Closely associated with this oxygenation event is the occurrence of decimeter-scale multicellular eukaryotes, suggesting a possible causal relationship between oxygenation and early evolution of eukaryotes (Zhu et al., 2016; Zhang et al., 2018; Shang et al., 2019).

One of the intriguing phenomena for the ~1.57 Ga oxygenation event is its transient nature: geochemical proxies indicative of oxygenation quickly return back to mid-Proterozoic background values (Shang et al., 2019; Xie et al., 2022). In spite of the general consensus that enhanced organic carbon/pyrite burial is the most efficient way for oxygen increase in Earth's surface environment

(Berner, 2003), the cause(s) for such transient oxygenation events in the mid-Proterozoic remain uncertain. Existing hypotheses for oxygen increase include enhanced nutrient supply from upwelling of deep, anoxic seawater (Wang et al., 2020) or from weathering of large igneous provinces (LIPs; Horton et al., 2015; Diamond et al., 2021), and volcanic SO_2 injection into ferruginous seawater that may have led to fast pyrite burial (Olson et al., 2019).

To better constrain the potential causes of the ~1.57 Ga oxygenation event, we investigated the mercury (Hg) enrichment and Hg isotopes (particularly ^{202}Hg and ^{199}Hg) from the middle Gaoyuzhuang Formation in North China where evidence for oxygen increase were reported (Shang et al., 2019). We first use the Hg enrichment and isotopes data as proxy to distinguish possible Hg sources – particularly those from LIPs (e.g., Percival et al., 2015; Grasby et al., 2019; Shen et al., 2019), hydrothermal emission (e.g., Jones et al., 2019), and terrestrial weathering input (Fan et al., 2021; Liu et al., 2021). In combination with I/(Ca+Mg), P concentration, Rb/Al, $_{Nd}$(t), and ^{13}C profiles from the same section, we then discuss the potential causes the transient oxygenation event at ~1.57 Ga.

2 Geological Setting

The Gaoyuzhuang Formation constitutes the basal stratigraphic unit of the Jixian Group (1600–1400 Ma) in North China and is dominated by dolostone and dolomitic limestone with a few of calcareous shale interbeds, which were interpreted to have deposited from deep subtidal to supratidal environments on the North China Platform (Zhang et al., 2018; Shang et al., 2019). The sedimentary succession is well preserved, with regional metamorphic grades generally below prehnite–pumpellyite facies (Chu et al., 2007). The Gaoyuzhuang Formation consists of four members (I–IV) and the oxygenation event was documented in the upper Member II to III (Shang et al., 2019).

The age of the Gaoyuzhuang Formation is constrained by zircon U-Pb ages of 1577 ± 12 Ma and 1560 ± 5 Ma from tuffaceous beds in the lower and upper Member III, respectively (Li et al., 2010; Tian et al., 2015). The oxygenation event reported by Shang et al. (2019) was estimated to be between ~1580 and ~1560 Ma in age, with its peak at ~1.57 Ga.

3 Materials and Methods

Carbonate samples were collected with meter-scale resolution from the middle Gaoyuzhuang Formation at the Gan'gou Village (40°39 35.05 N, 116°14 35.63 E), Yanqing County, ~160 km north of Beijing (Figure 1). The samples analyzed in this study are the same as those used for I/(Ca+Mg) analyses by Shang et al. (2019). Major elements (Fe, Al, P), total organic carbon (TOC), total sulfur (TS), $_{Nd}$(t), Hg concentration and Hg isotopes are further analyzed in this study. In addition, 57 calcareous shale and muddy carbonate samples were collected from the same section for Rb/Al analysis.

For major elements analysis, ~50 mg sample powder was dissolved in 250 mg

lithium metaborate at 990 °C for 20 min and then diluted to 100 mL by MQ before element measurement using Inductively Coupled Plasma Optical Emission Spectrometry (ICP-OES) at China University of Geosciences (Beijing). For TOC analysis, about 10 g sample powders were weighed, decarbonated with 10% HCl, rinsed by deionized water and dried. About 200 mg decarbonated residues were weighed and wrapped in tin capsules and analyzed using an Elementar Macro Cube element analyzer. For content of total sulfur (TS) analysis, ~25 mg sample powder without decarbonation was analyzed using an Elementar Macro Cube element analyzer. The relative analytical uncertainties for TOC and TS monitored by repetitive analyses of the reference material sulfanilamide are <0.5%. Mercury concentration was measured at the National Research Center for Geoanalysis, Beijing, on whole-rock powders using an AFS-830a mercury analyzer (atomic fluorescence spectrometer) with uncertainty <20%.

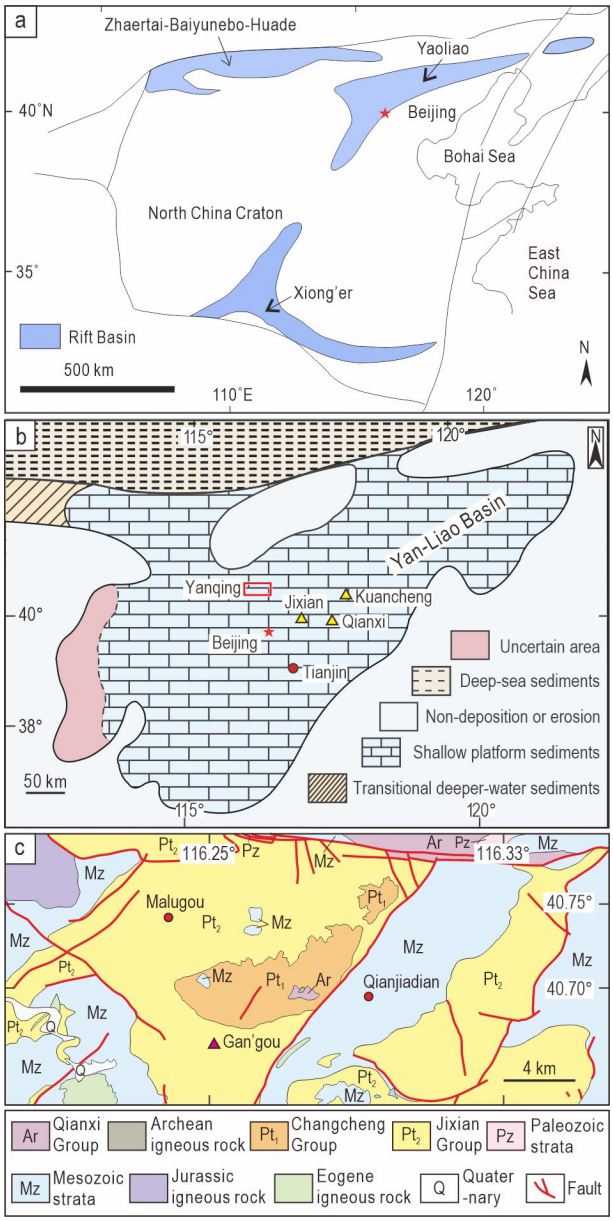

Figure 1. Geological setting of the studied area. (a) Distribution of the mid-Proterozoic rifts in North China (modified from Zhai and Liu, 2003). (b) A generalized Mesoproterozoic paleogeographic map of the central North China Platform (modified after Wang et al., 1985). (c) Simplified geological map of the study area, showing locality of the studied Gan'gou Section in Yanqing County, north of Beijing (modified from the 1:200,000 Geological Map of China, The China Geological Survey, 2013).

The methods for trace element analysis were adopted from Zhou et al. (2018). Approximately 25 mg sample powder for each sample was weighed out and dissolved using 1.5 mL HF and 0.5 mL HNO_3 in a Teflon bomb, and heated at 220 °C for 24 h. After evaporating sample solution to dryness on 170 °C hot plate, 0.5 mL HNO_3 was added, and repeated four times. After adding 2.5 mL of HNO_3, the Teflon bomb was sealed and heated at 150 °C for 4 h. After cooling, the solution was transferred to a PFA vial, and diluted with MQ water to 25 mL. The trace elements were measured by PerkinElmer NexION 300Q inductively coupled plasma mass spectrometry (ICP-MS) at the National Research Center for Geoanalysis, Beijing. The accuracy for all ICP-MS analyses is better than 5−10% (relative) for analyzed elements.

A subset of samples ($n = 24$) were chosen for Hg isotope analysis at the State Key Laboratory of Environmental Geochemistry, Institute of Geochemistry (Chinese Academy of Sciences, Guiyang). Analytical method and processing procedure follow those of Fan et al. (2021). Hg in the samples was preconcentrated into 10 mL of 40% mixed acid solution (v/v, HNO_3/HCl = 2:1) using a double-stage combustion method developed for Hg isotope analysis (Sun et al., 2013). Immediately after the preconcentration, the trapping bottle and impinger were rinsed three times with 10 mL of Milli-Q water, which was then added into the trapping solution to yield an ultimate acid concentration of ~20%. The final solutions were kept in refrigerator at 2–4 °C until the Hg isotope analysis was performed. Hg isotope ratios were analyzed using cold vapor-multicollector inductively coupled plasma mass spectrometry (CV-MC-ICPMS, Nu Instruments, U.K.) (Fu et al., 2019). Isotopic ratios were corrected for mass bias by standard-sample-standard bracketing using the Standard Reference Material (SRM) 3133 from the National Institute of Standards and Technology (NIST). Mass-dependent fractionation (MDF) of Hg isotopes (^{202}Hg) was reported in standard notation relative to the NIST 3133 Hg standard: $^{202}\text{Hg} = [(^{202}\text{Hg}/^{198}\text{Hg})_{\text{sample}}/(^{202}\text{Hg}/^{198}\text{Hg})_{\text{standard}} - 1] \times 1000‰$. Mass-independent fractionation (MIF) of Hg isotopes was reported as $\Delta^{x}\text{Hg} = {}^{x}\text{Hg} - \times {}^{202}\text{Hg}$, where x is the mass number of Hg isotopes (199, 200, 201 and 204) and is a scaling factor calculated from kinetic mass dependent fractionation law (0.2520, 0.5024, 0.7520 and 1.493, respectively). Analytical uncertainty of the Hg isotopic analysis was monitored by repeated analysis of the UM-Almaden standard. The mean values of ^{202}Hg, Δ^{199}Hg, Δ^{200}Hg, Δ^{201}Hg and Δ^{204}Hg for the standard were $-0.51 \pm 0.12‰$, $-0.00 \pm 0.06‰$, $-0.02 \pm 0.07‰$, $-0.01 \pm 0.07‰$ and $-0.01 \pm 0.10‰$ (2SD, $n = 7$; Table S1), respectively, which are in perfect agreement with previously reported values (Blum & Bergquist, 2007).

For Nd isotope analysis, the trace element Sm and Nd were first determined following the method of Zhou et al. (2018). About 3 g sample powders were weighed, decarbonated with 10% HCl, rinsed by deionized water and dried, and then Sm and Nd concentrations in the decarbonated sample powders were determined. Nd isotopic compositions were determined at the National Research Center of Geoanalysis, Beijing. For the analysis, part of solutions for trace ele-

ment analysis containing about 200 ng Nd was taken out from the PFA bottle, and purified following the procedure of Makishima et al. (2008). In brief, the solution was dried and redissolved in 0.25 M HCl before being loaded onto an Ln-spec column to separate Nd. The Nd isotope ratios were analyzed using a MC-ICP-MS (Neptune Plus, Thermo Fisher Scientific, Germany). Calculated $^{143}Nd/^{144}Nd$ isotopic ratios were normalized to $^{146}Nd/^{144}Nd$ ratios of 0.7219, to correct for instrumental mass fractionation. The chondritic reference values used for $_{Nd}$ calculations are $^{143}Nd/^{144}Nd_{CHUR} = 0.512638$ (Goldstein et al., 1984), $^{147}Sm/^{144}Nd_{CHUR} = 0.1967$ (Jacobsen & Wasserburg, 1980), and the decay constant for ^{147}Sm was assumed to be 6.54×10^{-12} a^{-1} (Lugmair & Marti, 1978). Analyses of repeat analyses of standard BHVO-1 and BCR-2 yielded $^{143}Nd/^{144}Nd$ ratios of 0.512984 ± 0.000006 and 0.512626 ± 0.000006, respectively. Total Nd procedural blanks were <50 pg.

4 Results

The measured Hg abundance is persistently high (up to ~50 ppb) across the increased oxygenation interval marked by high I/(Ca+Mg), but it is low (<10 ppb) in the rest of the section (Figure 2; Table S2). Because anomalously low TOC could lead to false Hg/TOC anomalies, samples with TOC <0.2 wt% were removed from the reliable dataset (cf. Grasby et al., 2019). Similarly, samples with TS <0.05 wt% and Al <0.3 wt% were also excluded, because below these thresholds the Hg/TS or Hg/Al values are abnormally high and do not fall on a temporal trend.

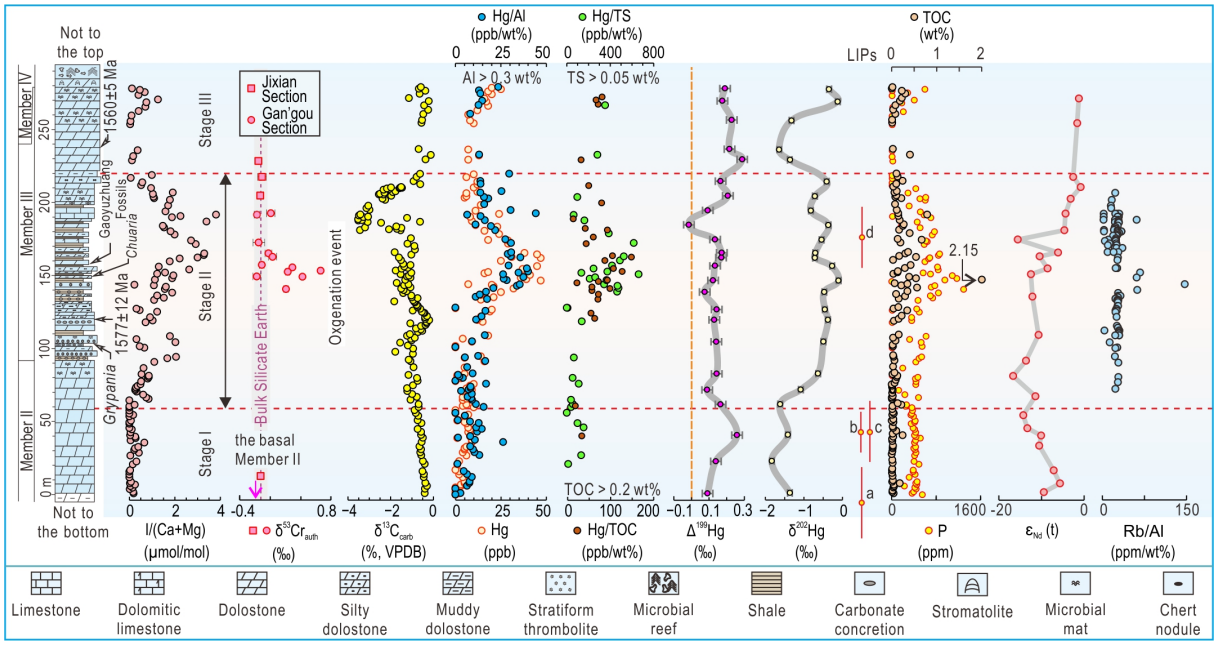

Figure 2. Geochemical profiles of the middle Gaoyuzhuang Formation at

Gan'gou (Yanqing County, north of Beijing), showing the geochemical trends of I/(Ca+Mg), $^{53}Cr_{auth}$, $^{13}C_{carb}$, Hg content, Hg/Al, Hg/TOC, Hg/TS, Δ^{199}Hg, ^{202}Hg, P and TOC content, $_{Nd}$(t) and Rb/Al. Positive excursions occurred in Hg, Hg/Al, Hg/TOC, Hg/TS, Hg/Al, ^{202}Hg, P, $_{Nd}$(t) and Rb/Al in stage II. Negative shift in Δ^{199}Hg are in well agreement with the increase in I/(Ca+Mg). LIPs and possible LIP fragments (Ernst et al., 2008): (**a**) 1595 ± 3.5 Ma, 0.059 MKm^2 dykes in Sweden; (**b**) 1592 ± 3 Ma sills in NW Laurentia; (**c**) 1592 ± 2 Ma, 0.131 MKm^2 mainly felsic volcanics in S Australia; (**d**) 1569 ± 3 Ma 0.021 MKm^2 dykes and sills in Scandinavia. Data of I/(Ca+Mg) and $^{13}C_{carb}$ are from Shang et al. (2019), data of $^{53}Cr_{auth}$ from Xie et al. (2022), while the others from this study. Some $^{53}Cr_{auth}$ data from the Jixian Section were also illustrated in this figure for display the secular variation (cf. Xie et al., 2022).

After normalized by Al, TOC and TS, the Hg peaks remain (Figure 2). The interval with high I/(Ca+Mg) up to ~3.5 mol/mol and positive $^{53}Cr_{auth}$ up to 0.66‰ in the Gaoyuzhuang Member III has apparently higher values of Hg/TOC (up to ~150 ppb/wt%), Hg/TFe (up to ~60 ppb/wt%), Hg/TS (up to ~600 ppb/wt%), Hg/Al (up to ~40 ppb/wt%), P (up to ~1200 ppm) and Rb/Al (up to ~150 ppm/wt%; Figure 2; Table S2 and Table S3) than those in the underlying and overlying intervals. The Hg concentrations show positive correlations with Al and TOC (Figures 3A and B), but not with TS (Figure 3C).

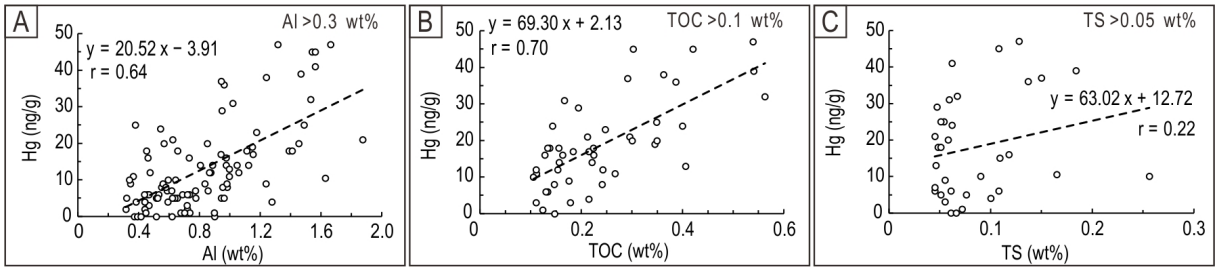

Figure 3. Cross plots showing the relationships between Hg abundance and other geochemical proxies. (a) Al vs. Hg. (b) TOC vs. Hg. (c) TS vs. Hg.

Mass-dependent fractionation (MDF) and mass-independent fractionation (MIF) of Hg isotopes (^{202}Hg and Δ^{199}Hg) show consistent and opposite trends with I/(Ca+Mg), respectively (Figure 2). Coupled with the increase of I/(Ca+Mg), ^{202}Hg exhibits a positive excursion from ~−1.5‰ (Stage I) to ~−0.50‰ (Stage II) and then back to ~−1.5‰ (Stage III). In contrast, Δ^{199}Hg shows low value of ~0.10‰ in Stages I and II, with a higher value of 0.26‰ in one sample in upper Stage I, and displays a positive shift to ~0.25‰ in Stage III (Figure 2; Table S4). Corresponding to Stages I and II, contemporaneous LIPs are documented from other continents but not known in North China (Ernst et al., 2008; Figure 2). Distinctively, $_{Nd}$(t) does not covary with Hg geochemistry but shows a negative shift from −5.8 to −14.4 in Stage I, then a positive shift from −16.7 to −0.9 in Stage II, and retains the high values

in stage III (Figure 2; Table S5). The peaks of I/(Ca+Mg) and Hg/TOC correspond to the low $_{Nd}(t)$ values around −10 and the peak of Rb/Al at ~150 ppm/wt% (Figure 2; Table S3; Table S5).

5 Discussion

5.1 Hg Enrichment across the ~1.57 Ga Oxygenation Event

The Hg enrichment accompanied with I/(Ca+Mg) peak implies that during the oxygenation event there was an increased Hg input or a more efficient Hg sink in the depositional environment. In marine environments, Hg can be scavenged to sediment by organic matter (Sanei et al., 2012), sulfides (Zheng et al., 2018; Shen et al., 2019) or clay minerals (Pruss et al., 2019). The positive correlations between Hg and Al, TOC and the lack of correlation between Hg and TS in our samples (Figure 3) suggest that Hg was likely removed from seawater by clay minerals and organic matter, but not by sulfide.

In the studied section, lithological changes toward the Hg peak were observed, and higher Hg concentration tended to occur in the intervals with increased shale and muddy dolostone layers (Figure 2). However, the significant enrichment in Hg (Hg/TOC at ~150 m) does not correspond to the conspicuous change in lithology, which is located at ~90 m around the Member II-III boundary (Figure 2), suggesting that changes in lithology and depositional rate may not be the major controlling factors on Hg enrichment. Thus, the Hg enrichment in the carbonates associated with the ~1.57 Ga oxygenation event was not caused by enhanced sink, but an increased Hg input to the shallow-marine environment.

5.2 Enhanced Weathering Input and Hg Anomalies

Hg sources in shallow marine depositional environments may include (1) atmospheric Hg from subaerial volcanic activity (e.g., Percival et al., 2015; Grasby et al., 2019), (2) riverine Hg input from oxidative weathering (e.g., Liu et al., 2021), (3) release from remineralization of organic matter or oxidation of DOC from deep seawater (e.g., Fan et al., 2021; Liu et al., 2021), and (4) hydrothermal input (Jones et al., 2019). Syn-depositional hydrothermal fluids can result in local sediment Hg enrichment up to 90 ppm (Jones et al., 2019). In our case, however, the lack of positive Eu anomalies throughout the middle-upper Gaoyuzhuang Formation (Zhang et al., 2018) does not support a significant source from hydrothermal fluids. Oxidation of DOC caused by the expansion of oxygenated seawater during the ~1.57 Ga oxygenation event (Shang et al., 2019) could potentially release DOC-bonded Hg into seawater. In this case, a negative shift in ^{202}Hg would be expected because DOC-bonded Hg commonly has low ^{202}Hg value, similar to that seen in the Ediacaran subsurface seawater (e.g., ^{202}Hg < –1.6‰; cf. Fan et al., 2021). The increase—rather than decrease—of ^{202}Hg from –1.5‰ to –0.5‰ toward the Hg/TOC peak and the lack of significant Hg/TOC change across the negative ^{13}C excursion interval in our samples (Figure 2) do not support DOC-bonded Hg as a main source either.

MIF and MDF isotope features of Hg can be used to distinguish the Hg sources from volcanic or continent weathering. Volcanic eruption, particularly that associated with LIP, is one of the major causes for Hg enrichment in sedimentary successions (e.g., Grasby et al., 2019). Volcanically emitted Hg(0) has no MIF (e.g., Δ^{199}Hg = 0‰); photo-oxidation of Hg(0) to Hg(II) will generate positive MIF, leaving a negative Δ^{199}Hg signal (Δ^{199}Hg < 0‰) in the residual Hg(0) pool and a positive Δ^{199}Hg signal (Δ^{199}Hg > 0‰) in reactive, water-soluble Hg(II) (Blum et al., 2014; Shen et al., 2022). As a result, marine sediments containing direct atmospheric Hg(II) deposition—such as those from open ocean environments—would have positive ^{199}Hg values (Shen et al., 2019, 2022); whereas terrestrial reservoirs such as plant biomass and soils that primarily accumulate atmospheric Hg(0) would show negative Δ^{199}Hg values (Blum et al., 2014).

The Δ^{199}Hg values from the Gaoyuzhuang Members II and III are all positive. Particularly, the interval with high Hg/TOC value in the studied section has a median Δ^{199}Hg value of 0.14‰ (Stage II in Figure 2), which is comparable to that of the pre-anthropogenic marine sediments dominated by atmospheric Hg(II) deposition (Δ^{199}Hg = 0.12 ± 0.05‰; Zheng et al., 2018). In contrast, Stage III has the highest Δ^{199}Hg value of 0.29‰ and Stage I has a high Δ^{199}Hg value of 0.26‰. Taking the Δ^{199}Hg data alone could have two possible interpretations: (1) the relatively lower Δ^{199}Hg values in Stage II represent the background values that may have captured atmospheric Hg(II) deposition, and the higher values in Stages III and I may have recorded signals from subaerial volcanic eruptions (cf. Grasby et al., 2017); or alternatively (2) the higher Δ^{199}Hg values in Stages III and I represented the background values, and the lower Δ^{199}Hg values in Stage II reflected the addition of terrestrial Hg input, with potential contributions from less aqueous photoreduction or enhanced Hg(0) deposition. The first scenario is not supported by the low Hg/TOC values in Stages III and I. Hence, the second scenario appears to be the most likely interpretation. In other words, enhanced continental weathering input rather than volcanic eruption has resulted in the lower Δ^{199}Hg and higher Hg/TOC values than the neighboring Stages I and III. However, this interpretation also requires a higher (than Phanerozoic) background Δ^{199}Hg value for the Mesoproterozoic marine Hg(II) reservoir.

Low atmospheric oxygen levels in Mesoproterozoic may have resulted in a pervasive anoxia in photic zone (e.g., Lyons et al., 2014), which could promote photoreduction of Hg(II) in the surface ocean. Aqueous photoreduction of Hg(II) in cloud droplets and surface waters generates large odd-MIF (e.g., Bergquist & Blum, 2007). If this was intensified in anoxic Mesoproterozoic surface oceans, it would increase the Δ^{199}Hg value of the marine Hg(II) reservoir. This explanation seems also to be supported by the high Δ^{199}Hg value in Late Archean sediments prior to the Great Oxidation Event (up to 0.6‰; e.g., Zerkle et al., 2020; Meixnerová et al., 2021). With a high background Δ^{199}Hg value in the marine Hg(II) reservoir, an increase in terrestrial Hg input would best explain the coupled rise of Hg/TOC and fall of Δ^{199}Hg in Stage II (Figure 2). As

there existed no land plant, the mid-Proterozoic terrestrial Hg reservoir was most likely dominated by Hg(II) retained in lithological crust (non-MIF) that would have ^{202}Hg ranging from –0.6‰ to –0.1‰ and Δ^{199}Hg value close to ~0‰, similar to those in volcanic ash and silicate rocks (cf. Zambardi et al., 2009; Fan et al., 2021; Liu et al., 2021). Hence, an increase in weathering input would result in lower Δ^{199}Hg but higher ^{202}Hg values in the marine Hg(II) reservoir. Thus, the most possible explanation for the lower Δ^{199}Hg, higher ^{202}Hg, and higher Hg/TOC values in Stage II than those in Stages I and III (Figure 2) is the enhanced continental weathering input. Decreased aqueous Hg(II) reduction in surface waters in response to oxygenation and increase of direct Hg(0) uptake (e.g., Jiskra et al., 2021) may have also contributed to the positive shift in ^{202}Hg and negative shift in Δ^{199}Hg during Stage II (Figure 2), but the current Hg geochemical data cannot distinguish the potential roles that these processes may have played in the oxidation event.

The enhanced weathering during Stage II is further supported by the increase of Rb/Al (Figure 2). Rb/Al ratio in fine grained sediments has been proposed as one of the most reliable proxies for intensity of chemical weathering (Bayon et al., 2022). Rb is enriched in K-feldspar, biotite and other mica minerals that are preferentially dissolved during the early stage of chemical weathering. The incongruent dissolution of biotite on continent could result in the high Rb/Al ratio in clay-size fraction of fine-grained sedimentary rocks, whereas accelerated feldspar weathering would derease the Rb/Al ratio (Bayon et al., 2021, 2022). Furthermore, Rb is depleted in seawater, diagenetic fluids, and metamorphic fluids (e.g., van de Kamp, 2016), and Rb in fine grained sediments would not be altered significantly by post-depositional processes. In our case, the peaks of Hg/TOC, P and I/(Ca+Mg), are well consistent with the peak of Rb/Al (Figure 2), suggesting that the enrichment of Hg and P, and the oxygenation of seawater were intimately connected to the enhanced chemical weathering of mica-rich rocks on continent.

5.3 Implication for Transient Oxygenation Event during the Mid-Proterozoic

Phosphorus is a bio-limiting nutrient and has played a pivotal role in modulating net primary productivity over geological timescales (Bjerrum & Canfield, 2002; Planavsky et al., 2010; Tang et al., 2022). During the ~1.57 Ga oxygenation, P content increased significantly as evidenced by its concentration and abundant apatite crystals observed in this interval (Figure 2; Figure 4 in Shang et al., 2019). The significant increase in P concentration (at ~60 m), however, is not in parallel with the conspicuous change in lithology at the Member II-III boundary (Figure 2), likely suggesting that the changes in lithology and depositional rate were not the major controls on P concentration.

Intensive continental weathering (e.g., Cox et al., 2018; Diamond et al., 2021), particularly the weathering of basaltic crust during the emplacement of LIPs (Horton, 2015), would significantly increase P supply to ocean, since mafic rocks have a much higher P content than those of ultramafic or felsic rocks (Cox et al. 2016). Considering that there is no significant LIPs reported in North China

during the oxygenation event, we argued that the elevated P input was most likely caused by enhanced continental weathering on newly exposed intermediate to mafic rocks. In this study, the $_{Nd}(t)$ was used to decipher the source rock of continental weathering, since mantle-derived mafic rocks commonly have relatively high $_{Nd}(t)$ values while crustal felsic rocks have very low $_{Nd}(t)$ values (e.g., Wu et al., 2005). During Paleoproterozoic, due to the contamination of crustal materials (possibly derived from subduction and/or collision) in North China Craton, the mantle-derived mafic rocks show slightly negative $_{Nd}(t)$ values (Wu et al., 2005). Therefore, the high $_{Nd}(t)$ value (up to −0.9) in Stage II likely reflects an enhanced weathering of (ultra)mafic rocks. It is worth to note that the peak of P is not associated with the highest $_{Nd}(t)$ value but with the medium $_{Nd}(t)$ values (~−10) (Figure 2), consistent with the weathering of intermediate to mafic source rocks (cf. Wu et al., 2005). This may imply that enhanced chemical weathering have supplied abundant P into the seawater (cf. Cox et al., 2016), which, via stimulating primary productivity and increased burial of organic matter (Figure 2; Reinhard et al., 2017; Laakso et al., 2020), may have eventually promoted the transient rise in oxygen levels at ~1.57 Ga.

It is noteworthy that the peaks of Rb/Al, Hg/TOC and P occur around 150 m, the spike of I/(Ca+Mg) is located at ~160 m, while the lowest $^{13}C_{carb}$ value appears at ~190 m (Figure 2) in the studied section. Such a temporal sequence likely indicates that (1) enhanced continent weathering first resulted in the increased P input to ocean, (2) the increased P input stimulated the primary productivity and enhanced oxygenation, and then (3) expansion of oxygenated seawater resulted in the oxidation of DOC, and excessive consumption of oxygen in seawater finally terminated the short oxygenation at ~220 m.

In Stage III, $_{Nd}(t)$ values remained high, while Rb/Al and I/(Ca+Mg) decreased. This likely suggested that though (ultra)mafic rocks were still the possible provenance, whereas the intensity of chemical weathering was subdued. This is likely one of the significant causes leading to a fall in oxygen concentration to the background level. The potential causes for the increase and decrease in chemical weathering intensity during Stage II and Stage III are not properly known. One plausible explanation would be the decrease in atmospheric CO_2 level and temperature due to the rapid consumption of CO_2 by chemical weathering during Stage II, which reduced the chemical weathering intensity during Stage III. The reduced weathering input, limited P recycling in ferruginous seawater conditions (Guilbaud et al., 2020; Laakso et al., 2020), and oxidation of DOC (Shang et al., 2019), may together have caused the rapid ending of mid-Proterozoic oxygenation events.

6 Conclusions

The ~1.57 Ga oxygenation event is coupled with Hg enrichment (Hg/TOC increase from ~20 to ~150 ppb/wt%), positive excursion of ^{202}Hg (~−1.5‰ to ~−0.5‰), negative shift in Δ^{199}Hg (~0.25‰ to ~0.10‰), increase of Rb/Al (~25 ppm/wt% to ~150 ppm/wt%) and positive shift of $_{Nd}(t)$ (−16.7 to −0.9). These can be well explained by an enhanced continent weathering of interme-

diate to mafic rocks. The enhanced weathering may have led to increase of nutrient inputs to the ocean, particularly P, thus accelerating primary productivity, organic matter burial and eventually a rise in oxygen level.

Acknowledgements

This research was supported by the National Key Research and Development Project of China (2020YFA0714803), the National Natural Science Foundation of China (Nos. 41930320, 41972028), the Key Research Program of the Institute of Geology & Geophysics, CAS (No. IGGCAS-201905), the Chinese "111" project (B20011) and the Fundamental Research Funds for the Central Universities (No. 292019093).

Conflict of Interest

The authors declare no conflict of interest relevant to this study.

Open reseach

Data supporting this study are available at https://doi.org/10.26022/IEDA/112274.

References

Bayon, G., Bindeman, I. N., Trinquier, A., Retallack, G. J., & Bekker, A. (2022). Long-term evolution of terrestrial weathering and its link to Earth's oxygenation. Earth and Planetary Science Letters, 584, 117490.https://doi.org/10.1016/j.epsl.2022.117490

Bayon, G., Freslon, N., Germain, Y., Bindeman, I. N., Trinquier, A., & Barrat, J. A. (2021). A global survey of radiogenic strontium isotopes in river sediments. Chemical Geology, 559, 119958. https://doi.org/10.1016/j.chemgeo.2020.119958

Bergquist, B. A., & Blum, J. D. (2007). Mass-dependent and-independent fractionation of Hg isotopes by photoreduction in aquatic systems. Science, 318(5849), 417–420. https://doi.org/10.1126/science.1148050

Berner, R. A. (2003). The long-term carbon cycle, fossil fuels and atmospheric composition. Nature, 426(6964), 323–326. https://doi.org/10.1038/nature02131

Bjerrum, C. J., & Canfield, D. E. (2002). Ocean productivity before about 1.9 Gyr ago limited by phosphorus adsorption onto iron oxides. Nature, 417(6885), 159–162. https://doi.org/10.1038/417159a

Blum, J. D., & Bergquist, B. A. (2007). Reporting of variations in the natural isotopic composition of mercury. Analytical and Bioanalytical Chemistry, 388(2), 353–359. https://doi.org/10.1007/s00216-007-1236-9

Blum, J. D., Sherman, L. S., & Johnson, M. W. (2014). Mercury isotopes in earth and environmental sciences. Annual Review of Earth and Planetary Sciences, 42, 249–269. https://doi.org/10.1146/annurev-earth-050212-124107

Canfield, D. E., Zhang, S., Frank, A. B., Wang, X., Wang, H., Su, J., et al. (2018). Highly fractionated chromium isotopes in Mesoproterozoic-aged shales and atmospheric oxygen. Nature Communications, 9(1), 1–11. https://doi.org/10.1038/s41467-018-05263-9

Chu, X., Zhang, T., Zhang, Q., & Lyons, T. W. (2007). Sulfur and carbon isotope records from 1700 to 800 Ma carbonates of the Jixian section, northern China: Implications for secular isotope variations in Proterozoic seawater and relationships to global supercontinental events. Geochimica et Cosmochimica Acta, 71(19), 4668–4692. https://doi.org/10.1016/j.gca.2007.07.017

Cox, G. M., Halverson, G. P., Stevenson, R. K., Vokaty, M., Poirier, A., Kunzmann, M., Li, Z. X., Denyszyn, S. W., Strauss, J. V., & Macdonald, F. A., (2016). Continental flood basalt weathering as a trigger for Neoproterozoic Snowball Earth. Earth and Planetary Science Letters, 446, 89–99. https://doi.org/10.1016/j.epsl.2016.04.016

Cox, G. M., Lyons, T. W., Mitchell, R. N., Hasterok, D., & Gard, M. (2018). Linking the rise of atmospheric oxygen to growth in the continental phosphorus inventory. Earth and Planetary Science Letters, 489, 28–36. https://doi.org/10.1016/j.epsl.2018.02.016

Diamond, C. W., Ernst, R. E., Zhang, S.-H., & Lyons, T. W. (2021). Breaking the Boring Billion: A Case for Solid-Earth Processes as Drivers of System-Scale Environmental Variability During the Mid-Proterozoic. Large Igneous Provinces: A Driver of Global Environmental and Biotic Changes, 487–501. https://doi.org/10.1002/9781119507444.ch21

Ernst, R. E., Wingate, M. T. D., Buchan, K. L., & Li, Z. X. (2008). Global record of 1600–700 Ma Large Igneous Provinces (LIPs): implications for the reconstruction of the proposed Nuna (Columbia) and Rodinia supercontinents. Precambrian Research, 160(1–2), 159–178. https://doi.org/10.1016/j.precamres.2007.04.019

Fan, H., Fu, X., Ward, J. F., Yin, R., Wen, H., & Feng, X. (2021). Mercury isotopes track the cause of carbon perturbations in the Ediacaran ocean. Geology, 49(3), 248–252. https://doi.org/10.1130/G48266.1

Fu, X., Zhang, H., Feng, X., Tan, Q., Ming, L., Liu, C., & Zhang, L. (2019). Domestic and transboundary sources of atmospheric particulate bound mercury in remote areas of China: evidence from mercury isotopes. Environmental Science & Technology, 53(4), 1947–1957. https://doi.org/10.1021/acs.est.8b06736

Goldstein, S.L., O'nions, R.K., & Hamilton, P.J. (1984). A Sm-Nd isotopic study of atmospheric dusts and particulates from major river systems. Earth and planetary Science letters, 70, 221–236. https://doi.org/10.1016/0012-821X(84)90007-4

Grasby, S. E., Shen, W., Yin, R., Gleason, J. D., Blum, J. D., Lepak, R. F., et al. (2017). Isotopic signatures of mercury contamination in latest Permian

oceans. Geology, 45(1), 55–58. https://doi.org/10.1130/G38487.1

Grasby, S. E., Them II, T. R., Chen, Z., Yin, R., & Ardakani, O. H. (2019). Mercury as a proxy for volcanic emissions in the geologic record. Earth-Science Reviews, 196, 102880. https://doi.org/10.1016/j.earscirev.2019.102880

Guilbaud, R., Poulton, S. W., Thompson, J., Husband, K. F., Zhu, M., Zhou, Y., et al. (2020). Phosphorus-limited conditions in the early Neoproterozoic ocean maintained low levels of atmospheric oxygen. Nature Geoscience, 13(4), 296–301. https://doi.org/10.1038/s41561-020-0548-7

Horton, F. (2015). Did phosphorus derived from the weathering of large igneous provinces fertilize the Neoproterozoic ocean? Geochemistry, Geophysics, Geosystems, 16(6), 1723–1738. https://doi.org/10.1002/2015GC005792

Jacobsen, S.B., & Wasserburg, G.J., (1980). Sm-Nd isotopic evolution of chondrites. Earth and Planetary Science Letters, 50, 139–155. https://doi.org/10.1016/0012-821X(80)90125-9

Jiskra, M., Heimbürger-Boavida, L. E., Desgranges, M.-M., Petrova, M. V., Dufour, A., Ferreira-Araujo, B., et al. (2021). Mercury stable isotopes constrain atmospheric sources to the ocean. Nature, 597(7878), 678–682. https://doi.org/10.1038/s41586-021-03859-8

Jones, M. T., Percival, L. M., Stokke, E. W., Frieling, J., Mather, T. A., Riber, L., et al. (2019). Mercury anomalies across the Palaeocene–Eocene thermal maximum. Climate of the Past, 15(1), 217–236. https://doi.org/10.5194/cp-15-217-2019

Laakso, T,A,, Sperling, E.A., Johnston, D.T., Knoll, A.H. (2020). Ediacaran reorganization of the marine phosphorus cycle. Proceedings of The National Academy of Sciences, USA, 117, 11961–11967. https://doi.org/10.1073/pnas.1916738117.

Li, H., Zhu, S., Xiang, Z., Su, W., Lu, S., Zhou, H., et al. (2010). Zircon U–Pb dating on tuff bed from Gaoyuzhuang Formation in Yanqing, Beijing: Further constraints on the new subdivision of the Mesoproterozoic stratigraphy in the northern North China Craton: Acta Petrologica Sinica, 2(7), 2131–2140 (in Chinese with English abstract). https://doi.org/000-0569/2010/026(07)-2131-40

Liu, Z. R. R., Zhou, M. F., & Wang, W. (2021). Mercury anomalies across the Ediacaran–Cambrian boundary: Evidence for a causal link between continental erosion and biological evolution. Geochimica et Cosmochimica Acta, 304, 327–346. https://doi.org/10.1016/j.gca.2021.04.011

Lugmair, G.W., & Marti, K., (1978). Lunar initial $^{143}Nd/^{144}Nd$: differential evolution of the lunar crust and mantle. Earth and Planetary Science Letters, 39, 349–357. https://doi.org/10.1016/0012-821X(78)90021-3

Lyons, T.W., Reinhard, C.T. & Planavsky, N.J., (2014). The rise of oxygen in Earth's early ocean and atmosphere. Nature, 506, 307 315.

https://doi.org/10.1038/nature13068

Makishima, A., Nath, B.N., & Nakamura, E., (2008). New sequential separation procedure for Sr, Nd and Pb isotope ratio measurement in geological material using MC-ICP-MS and TIMS. Geochemical Journal, 42, 237–246. https://doi.org/10.2343/geochemj.42.237

Meixnerová, J., Blum, J.D., Johnson, M.W., Stüeken, E.E., Kipp, M.A., Anbar, A.D., & Buick, R. (2021). Mercury abundance and isotopic composition indicate subaerial volcanism prior to the end-Archean "whiff" of oxygen. Proceedings of the National Academy of Sciences, 118, e2107511118. https://doi.org/10.1073/pnas.2107511118

Olson, S. L., Ostrander, C. M., Gregory, D. D., Roy, M., Anbar, A. D., & Lyons, T. W. (2019). Volcanically modulated pyrite burial and ocean–atmosphere oxidation. Earth and Planetary Science Letters, 506, 417–427. https://doi.org/10.1016/j.epsl.2018.11.015

Percival, L. M. E., Witt, M. L. I., Mather, T. A., Hermoso, M., Jenkyns, H. C., Hesselbo, S. P., et al. (2015). Globally enhanced mercury deposition during the end-Pliensbachian extinction and Toarcian OAE: A link to the Karoo–Ferrar Large Igneous Province. Earth and Planetary Science Letters, 428, 267–280. https://doi.org/10.1016/j.epsl.2015.06.064

Planavsky, N. J., Reinhard, C. T., Wang, X., Thomson, D., McGoldrick, P., Rainbird, R. H., et al. (2014). Low Mid-Proterozoic atmospheric oxygen levels and the delayed rise of animals. Science, 346(6209), 635–638. https://doi.org/10.1126/science.1258410

Planavsky, N. J., Rouxel, O. J., Bekker, A., Lalonde, S. V., Konhauser, K. O., Reinhard, C. T., & Lyons, T. W. (2010). The evolution of the marine phosphate reservoir. Nature, 467(7319), 1088–1090. https://doi.org/10.1038/nature09485

Reinhard, C. T., Planavsky, N. J., Gill, B. C., Ozaki, K., Robbins, L. J., Lyons, T. W., Fischer, W. W., Wang, C., Cole, D. B., & Konhauser, K. O. (2017). Evolution of the global phosphorus cycle. Nature, 541, 386. https://doi.org/10.1038/nature20772.

Sanei, H., Grasby, S. E., & Beauchamp, B. (2012). Latest Permian mercury anomalies. Geology, 40(1), 63–66. https://doi.org/10.1130/G32596.1

Shang, M., Tang, D., Shi, X., Zhou, L., Zhou, X., Song, H., & Jiang, G. (2019). A pulse of oxygen increase in the early Mesoproterozoic ocean at ca. 1.57–1.56 Ga. Earth and Planetary Science Letters, 527, 115797. https://doi.org/10.1016/j.epsl.2019.115797

Shen, J., Algeo, T. J., Planavsky, N. J., Yu, J., Feng, Q., Song, H., et al. (2019). Mercury enrichments provide evidence of Early Triassic volcanism following the end-Permian mass extinction. Earth-Science Reviews, 195, 191–212. https://doi.org/10.1016/j.earscirev.2019.05.010

Shen, J., Yin, R., Algeo, T. J., Svensen, H.H., & Schoepfer, S.D. (2022). Mercury evidence for combustion of organic-rich sediments during the end-Triassic crisis. *Nature Communications,* **13**, 1307. https://doi.org/10.1038/s41467-022-28891-8

Sun, R., Enrico, M., Heimbürger, L. E., Scott, C., & Sonke, J. E. (2013). A double-stage tube furnace—acid-trapping protocol for the pre-concentration of mercury from solid samples for isotopic analysis. Analytical and Bioanalytical Chemistry, 405(21), 6771–6781. https://doi.org/10.1007/s00216-013-7152-2

Tang, D., Xie, B., Shi, X., & Zhou, X. (2022). Low level of phosphorous concentration in terminal Paleoproterozoic shallow seawater: Evidence from Chuanlinggou ironstone on North China Platform. Precambrian Research, 370, 106554. https://doi.org/10.1016/j.precamres.2021.106554

Tian, H., Zhang, J., Li, H., Su, W., Zhou, H., Yang, L., et al. (2015). Zircon LA-MC-ICPMS U-Pb dating of tuff from Mesoproterozoic Gaoyuzhuang Formation in Jixian County of North China and its geological significance. Acta Geoscientica Sinica, 36(5), 647–658(in Chinese with English abstract). https://doi.org/10.3975/cagsb.2015.05.12

van de Kamp, P. C. (2016). Potassium distribution and metasomatism in pelites and schists: how and when, relation to postdepositional events. Journal of Sedimentary Research, 86(6), 683–711. https://doi.org/10.2110/jsr.2016.44

Wang, H., Chu, X., Liu, B., Hou, H., & Ma, L., (1985), Atlas of the Palaeogeography of China. Cartographic Publishing House, Beijing (in Chinese and English, 143 pp.).

Wang, H., Zhang, Z., Li, C., Algeo, T. J., Cheng, M., & Wang, W. (2020). Spatiotemporal redox heterogeneity and transient marine shelf oxygenation in the Mesoproterozoic ocean. Geochimica et Cosmochimica Acta, 270, 201–217. https://doi.org/10.1016/j.gca.2019.11.028

Wu, F., Zhao, G., Wilde, S. A., & Sun, D. (2005). Nd isotopic constraints on crustal formation in the North China Craton. Journal of Asian Earth Sciences, 24(5), 523–545. https://doi.org/10.1016/j.jseaes.2003.10.011

Xie, B., Zhu, J., Wang, X., Xu, D., Zhou, L., Zhou, X., Shi, X., & Tang, D., (2022). Mesoproterozoic oxygenation event: from shallow marine to atmosphere. GSA Bulletin, https://doi.org/10.1130/B36407.1.

Zambardi, T., Sonke, J. E., Toutain, J. P., Sortino, F., & Shinohara, H. (2009). Mercury emissions and stable isotopic compositions at Vulcano Island (Italy). Earth and Planetary Science Letters, 277(1–2), 236–243. https://doi.org/10.1016/j.epsl.2008.10.023

Zerkle, A. L., Yin, R., Chen, C., Li, X., Izon, G. J., & Grasby, S. E. (2020). Anomalous fractionation of mercury isotopes in the Late Archean atmosphere. Nature communications, 11(1), 1709. https://doi.org/10.1038/s41467-020-15495-3

Zhai, M., & Liu, W. (2003). Palaeoproterozoic tectonic history of the North China craton: a review. Precambrian Research, 122(1–4), 183–199. https://doi.org/10.1016/S0301-9268(02)00211-5

Zhang, K., Zhu, X., Wood, R. A., Shi, Y., Gao, Z., & Poulton, S. W. (2018). Oxygenation of the Mesoproterozoic ocean and the evolution of complex eukaryotes. Nature Geoscience, 11(5), 345–350. https://doi.org/10.1038/s41561-018-0111-y

Zhang, S., Wang, X., Wang, H., Bjerrum, C. J., Hammarlund, E. U., Costa, M. M., et al. (2016). Sufficient oxygen for animal respiration 1,400 million years ago. Proceedings of the National Academy of Sciences, 113(7), 1731–1736. https://doi.org/10.1073/pnas.1523449113

Zheng, W., Demers, J. D., Lu, X., Bergquist, B. A., Anbar, A. D., Blum, J. D., & Gu, B. (2018). Mercury stable isotope fractionation during abiotic dark oxidation in the presence of thiols and natural organic matter. Environmental Science & Technology, 53(4), 1853–1862. https://doi.org/10.1021/acs.est.8b05047

Zhou, L.M., Wang, R., Hou, Z.Q., Li, C., Zhao, H., Li, X.W., & Qu, W.J. (2018). Hot Paleocene-Eocene Gangdese arc: Growth of continental crust in southern Tibet. Gondwana Research, 62, 178–197. https://doi.org/10.1016/j.gr.2017.12.011

Zhu, S., Zhu, M., Knoll, A. H., Yin, Z., Zhao, F., Sun, S., et al. (2016). Decimetre-scale multicellular eukaryotes from the 1.56-billion-year-old Gaoyuzhuang Formation in North China. Nature Communications, 7(1), 1–8. https://doi.org/10.1038/ncomms11500

Supporting Information

Table S1. Mercury isotopes of the reference NIST3177

Table S2. Geochemical data from the carbonates of the Gaoyuzhuang Formation at Gan'gou, northern suburb of Beijing.

Table S3 Geochemical data of calcareous shale and muddy carbonates of the Gaoyuzhuang Formation at Gan'gou, northern suburb of Beijing

Table S4. Mercury isotopes measured from the carbonate samples of the Gaoyuzhuang Formation.

Table S5. $_{\mathrm{Nd}}(\mathrm{t})$ measured from siliciclastic fraction of the carbonate samples of the Gaoyuzhuang Formation